ULTRASOUND STRAIN IMAGING WITH NULL SUBTRACTION AND CODED PLANE WAVES

Bingze Dai, *Student Member, IEEE*, Zhengchang Kou, *Member, IEEE*, Jiajing Zhang, Haotian Guan, Michael L. Oelze, *Senior Member, IEEE* and Wei-Ning Lee, *Senior Member, IEEE*

***Abstract*— Accurate displacement estimation is central to ultrasound strain imaging, which provides a full description of a 2D/3D deformation field to infer elasticity and detect tissue abnormalities. However, lateral displacement estimation has been the major bottleneck, especially with high frame rate requirements, due to inferior spatial resolution, low sampling, and the lack of phase information in that direction. This study focuses on enhancing lateral displacement estimation by improving the lateral resolution of ultrasound multiangle plane-wave imaging through a nonlinear beamformer, Incoherent Compounding Null Subtraction Imaging (IC-NSI). While IC-NSI effectively reduces both main lobe width and secondary lobe levels, its limited penetration depth and reduced speckle coherence are detrimental to tissue motion estimation. We hereby propose to improve the signal-to-noise ratio (SNR) and thus the penetration depth by integrating cascaded dual-polarity waves (CDW) into IC-NSI. We evaluate the feasibility and performance of IC-NSI, with and without CDW, for tissue displacement estimation through Field II and COMSOL simulations of deforming tubes, phantom experiments, and an *in vivo* study of the human common carotid artery. Both in silico and *in vivo* carotid ultrasound images obtained by the proposed method exhibited ∼40% improvement in lateral resolution compared with those by coherent plane wave compounding (CPWC). In phantom experiments, the sonographic SNR improved by 14∼17 dB across depths of 20 to 40 mm and had a 32% reduction in mean absolute error in lateral motion estimation in a controlled linear translation scenario. In simulations, our method achieved 13% higher estimation accuracy in lateral displacement under varying strain conditions compared to CPWC. These results demonstrated the conceptual and computational simplicity of the proposed method for high quality ultrasound strain imaging of thin biological structures.**

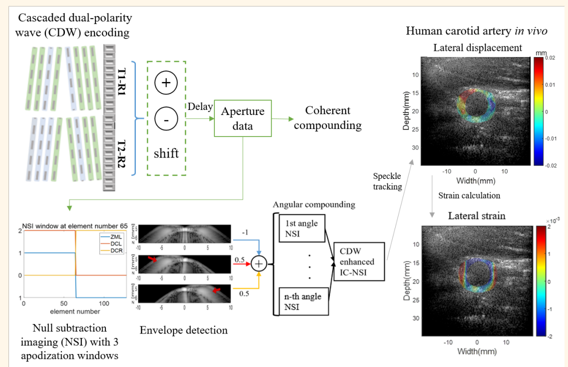

***Index Terms*— Coded excitation, null subtraction imaging, plane wave, speckle tracking, ultrasound strain imaging**

I. INTRODUCTION

ULTRASOUND strain imaging (USI), which aids in inferring mechanical properties, has had versatile clinical applications since its emergence a few decades ago [1]–[3]. Those applications aim to detect pathological changes in various biological soft tissues, such as breast [4], liver [5], [6], kidney [7], heart [8], [9], and blood vessels [10] as well as dynamics of skeletal muscle [11], [12], cardiac muscle [13], [14], vascular muscle [15], and tendons [16]. Ultrasound strain imaging is generally a two-step technique: 1) estimation of tissue displacement between pre- and post-deformed ultrasound signals, which can be radio-frequency (RF), analytical, or envelope data, and 2) calculation of strains, strain rates, or strain time constants [17]. Reliable clinical diagnosis requires high quality USI.

The quality of USI is tightly linked to the quality of acquired ultrasound image data via tailored speckle tracking (or motion estimation) algorithms [18]. Optimal spatial and temporal resolutions and high signal-to-noise ratio (SNR) of ultrasound images are pivotal for accurate depiction of fast tissue dynamics and reliable performance of a suitable strain estimator in eliminating noise and artifacts [19]. The interplay between the aforementioned imaging and algorithmic factors hinders the utility of USI in clinically challenging scenarios, such as acoustic attenuation in deep tissue characterization, geometrical or angle-dependent effect on polar strain calculation in cardiac strain imaging [20], and resolution limit in thin-walled structures, such as the abdominal aorta [21].

In USI, estimating lateral displacement poses significantly greater challenges than estimating axial displacement. Inferior

This work was supported by the Hong Kong Health and Medical Research Fund (08192616). (Corresponding author: Wei-Ning Lee.)

Bingze Dai, Jiajing Zhang, Haotian Guan, and Wei-Ning Lee are with Department of Electrical and Electronic Engineering, The University of Hong Kong, Hong Kong. (e-mail: bingzed, jiajingz, ght09@connect.hku.hk, wnlee@hku.hk). Zhengchang Kou and M.L. Oelze are affiliated with the Beckman Institute for Advanced Science and Technology, University of Illinois at Urbana-Champaign, Urbana, IL 61820 USA (email: zkou2@illinois.edu; oelze@illinois.edu), M.L. Oelze is also with Department of Electrical and Computer Engineering, Carle Illinois College of Medicine, and Department of Bioengineering at University of Illinois at Urbana-Champaign.

Highlights

- **The seamless integration of Cascaded Dual Polarity Coded Excitation (CDW) with Incoherent Compounding Null Subtraction Imaging (IC-NSI) enhances lateral resolution and sonographic signal-to-noise ratio, both of which are crucial for ultrasound speckle tracking and subsequent strain imaging.**
- **Performance evaluation resulted in ∼40% improvement in lateral resolution (in silico/*in vivo*), 14∼17 dB gain in sonographic SNR across depths, and 32% reduction in lateral displacement estimation errors in controlled phantom experiments, establishing IC-NSI with CDW as a synergistic, computationally efficient alternative to CPWC.**
- **The integration of IC-NSI and CDW enables more accurate ultrasound displacement and strain imaging of thin-walled structures, like blood vessels, improving clinical diagnostics in cardiovascular applications.**

resolution and a lower sampling rate in the lateral direction, resulting from the absence of a carrier signal compared to the axial direction, can lead to artifacts such as peak hopping and jitter [22], [23]. In continuum mechanics, shear strain is derived from both lateral and axial displacement components. Under finite deformation conditions, the lateral displacement component also contributes to the axial strain. Therefore, the accuracy and precision of lateral displacement estimation are critical for ensuring the overall reliability of USI [13], [24].

Numerous efforts to improve the performance of USI primarily fall into two categories: motion estimation [25] and direct strain estimation. The first category generally includes correlation and iterative correlation-based techniques [26]–[29], optical flow-based estimation [30], regularization strategies [31]–[36], machine learning-based methods [37]–[41], physics-based models [42]–[45], and techniques aimed at improving transmission sequence [46]–[48]. These methods are focused on optimizing spatial resolution, SNR, and tissue dynamics with each algorithm tailored to address specific aspects of these parameters. However, a common challenge shared by these techniques is their high computational complexity. Direct strain estimation [49] bypasses motion estimation and directly estimates tissue deformation from RF data.

In USI of dynamic tissues, a high frame rate is essential for capturing rapid physiological events. However, this often sacrifices spatial resolution and SNR, thereby compromising the quality of USI. In linear array imaging, coherent plane-wave compounding (CPWC) [50] is a prevalent method to achieve two-way focusing at frame rates higher than 1000 frames/second, providing a large field of view with image quality similar to conventional beamforming methods. It allows for more accurate strain estimation compared to conventional single-focused wave imaging [15]. While achieving a desired high frame rate, CPWC forms images by tuning the number of steered plane waves. Image quality is inevitably degraded to gain frame rate, resulting in diminished spatial resolution, SNR, larger side lobes, and reduced image contrast, all of which can impact local strain estimation.

The limitations of lateral resolution intrinsic to ultrasound imaging have prompted researchers to explore adaptive beamforming techniques originally developed for focused ultrasound systems. These techniques, such as Generalized Coherence Factor (GCF) [51], Minimum Variance (MV) [52], Delay Multiply and Sum (DMAS) [53], and p-th Root Delay and Sum (p-DAS) [54], can improve spatial resolution in CPWC. Nonetheless, these methods are accompanied by varying degrees of distortion of speckle patterns and an increase in computational cost. Both speckle coherence and computational efficiency are key considerations in motion estimation and strain imaging tasks. Therefore, to synergistically achieve the desired frame rate, preserve speckle coherence for displacement estimation, and improve lateral resolution in CPWC, it is imperative to explore alternative image formation methods.

This study therefore aims to tackle the fundamental challenge in ultrasound strain imaging: lateral displacement estimation. We hereby propose to improve lateral resolution and sonographic SNR for USI by combining Null Subtraction Imaging (NSI) [55] and Cascaded Dual-Polarity Waves (CDW) [56]. Unlike the aforementioned nonlinear beamformers, NSI is a nonlinear beamforming technique that enhances lateral resolution through a tunable DC offset, enabling control over the trade-off between spatial resolution and speckle pattern preservation. While NSI achieves this with lower computational cost than other non-linear beamformers, it reduces SNR. Furthermore, its feasibility in displacement estimation and strain imaging tasks remains unexplored. To mitigate the SNR limitation of NSI, we propose using CDW, a linear coded excitation technique that enhances sonographic SNR and thus penetration depth. To further enhance contrast, we employ incoherent NSI with multiple angled plane waves. By integrating NSI and CDW, we aim to improve lateral displacement and strain estimation without compromising frame rates or computational efficiency for USI.

The first application of the proposed method is on the carotid artery. The carotid arterial wall is typically approximately one-millimeter thick and interfaces with the blood, thus presenting strong side lobes and reverberations. The feasibility and performance of the proposed method is evaluated through finite-element and Field II simulations of a thin-walled tubular structure, an *in vitro* tissue-mimicking quality assurance phantom, and *in vivo* human common carotid artery.

The remainder of this paper is organized as follows. Section II describes how to leverage NSI and CDW to improve lateral displacement estimation and 2D strain imaging. Section III details computer simulations as well as *in vitro* and *in vivo* experiments. Section IV presents the *in silico*, *in vitro* and *in vivo* results and comparison with CPWC, the benchmark method. Section V discusses the results and their implications and suggests future research directions. Section VI concludes the work.

II. Methods

The accuracy of 2D displacement and strain estimation is fundamentally governed by the Cramér-Rao lower bound (CRLB), which establishes that estimation variance depends on both spatial resolution and SNR [57], [58]. Unbiased estimation requires optimization of both resolution and SNR. This principle underpins our co-design of CDW (Fig. 1(a)) and incoherent compounding Null Subtraction Imaging (IC-NSI) (Fig. 1(b)). The full CRLB derivation is provided in Appendix A, showing how pulse characteristics and deformation parameters jointly determine the theoretical limits of ultrasound strain imaging performance.

A. Null Subtraction Imaging (NSI)

1) Standard NSI: Null subtraction imaging utilizes three parallel apodization windows, including a zero-mean (ZM) window and two apodization windows with a DC offset on the ZM window, on the receive aperture to reduce sidelobe and grating lobe levels while narrowing the main lobe width [55], [59]. The step by step procedure of NSI for single-angle plane wave imaging is as follows:

Step 1. Calculate ZM apodization window. The ZM apodization consists of weights with equal numbers of +1 and -1 on either half of the receive sub-aperture and is defined as

$$A_{ZM,i} = \begin{cases} -1, & 1 \leq i < \frac{N}{2} \\ 1, & \frac{N}{2} \leq i \leq N \end{cases}, \tag{1}$$

where $A_{ZM,i}$ is the zero-mean apodization weight for element i, and N is the number of elements in an ultrasound array.

Step 2. Generate two apodization windows with a DC offset. The second apodization adds a constant DC offset, dc, to $A_{ZM,i}$ and is defined as

$$A_{DCL,i} = A_{ZM,i} + dc, \tag{2}$$

and the third apodization, A_{DCR}, is a left-right flipped version of the second at the null point (Fig. 1(b)).

Step 3. Following receive beamforming based on delay-and-sum and the three distinct apodization windows, an NSI image is generated by subtracting the zero-mean apodized image from the mean of two apodized images as follows:

$$E_{NSI} = \frac{E_{DCL} + E_{DCR}}{2} - E_{ZM}, \tag{3}$$

where E_{NSI} is the NSI envelope image, E_{ZM} is the zero-mean envelope image, and E_{DCL} and E_{DCR} are the two DC offset envelope images. The NSI image is subsequently normalized, log compressed, and displayed in gray scale.

2) Incoherent NSI (IC-NSI): Incoherent Compounding for Null Subtraction Imaging (IC-NSI) applies the NSI beamforming process independently to the raw channel data of each plane-wave angle to generate a set of high-resolution, high-contrast envelope images. These individual NSI envelope images are then compounded incoherently (i.e., averaged) to produce the final output. The primary motivation for this approach is to harness the resolution and contrast benefits of NSI while mitigating its primary drawback for displacement estimation: the degradation of speckle pattern [55].

This study first examined the effect of IC-NSI with varying DC offsets (1, 0.1, and 0.01) on speckle coherence for speckle tracking (i.e., displacement estimation) through phantom experiments using a pure translation scheme. The reliability of speckle tracking was quantified using normalized cross-correlation coefficients. The result showed that DC values of 0.1 and 0.01 could not preserve speckle coherence to the extent that reliable speckle tracking was required. This work hence proposed to use IC-NSI with DC offset = 1 for high-frame-rate imaging with plane waves to improve lateral resolution and contrast from NSI without compromising speckle coherence for speckle tracking.

B. Cascaded Dual-polarity Wave (CDW)

Cascaded dual-polarity wave (CDW) is a coded excitation method that transmits a long pulse which contains N ($N = 2^k$, $k = 0, 1, 2, \ldots$) cascaded waves with short time intervals and polarity coefficients of +1 and -1. Slightly different from the original CDW design for plane wave imaging, each transmission only transmits single-angle plane waves; in reception, backscattered signals from each transmit event are received as R1 and R2 signals from the same angle (Fig. 1(a)). A linear decoding scheme comprised of addition, subtraction, and delay operations was directly implemented on the received raw signals (i.e., channel data) to recover N times higher backscattered signal intensity to gain SNR of $10 \times log_{10}(N)$ dB without sacrificing frame rates prior to beamforming. Interested readers may refer to this coding strategy in greater detail in the work of Zhang et al. [56].

This study showcases the 16-digit (N=16) CDW sequence. The polarity of the first transmission event T1 is $[+1+1+1-1+1+1-1+1+1-1+1+1+1-1-1-1]$, and the second transmission event T2 is $[+1+1+1-1-1-1+1-1+1-1+1+1-1+1+1+1]$. Their respective reception events are R1 and R2. After CDW decoding with $log_2(N) = 4$ rounds of addition, subtraction, and delay operations, the decoded signals for R1 and R2 are equivalent to their corresponding single-cycle waves with a 16-fold amplitude.

C. Workflow of CDW-enhanced IC-NSI

Figure 1 shows the workflow of the proposed method. First, multiangle CDW coded plane waves are transmitted. The received backscattered signals are decoded to obtain high SNR channel data. Then, a corresponding delay map is calculated. The high SNR channel data are beamformed using DAS and IC-NSI with the same delay map and f-number = 1 to obtain CDW enhanced CPWC and IC-NSI images, respectively. Conventional CPWC and IC-NSI images can also be obtained by transmitting plane waves without code excitation. Note that the beamformed data after IC-NSI are envelope data.

D. Performance evaluation

Metrics adopted in this study for ultrasound image quality evaluation include contrast ratio (CR), contrast-to-noise ratio (CNR), and lateral beamwidth. The lateral resolution is evaluated by measuring the full width at half maximum (FWHM).

This article has been accepted for publication in IEEE Transactions on Ultrasonics. This is the author's version which has not been fully edited and
content may change prior to final publication. Citation information: DOI 10.1109/TUSON.2025.3649027

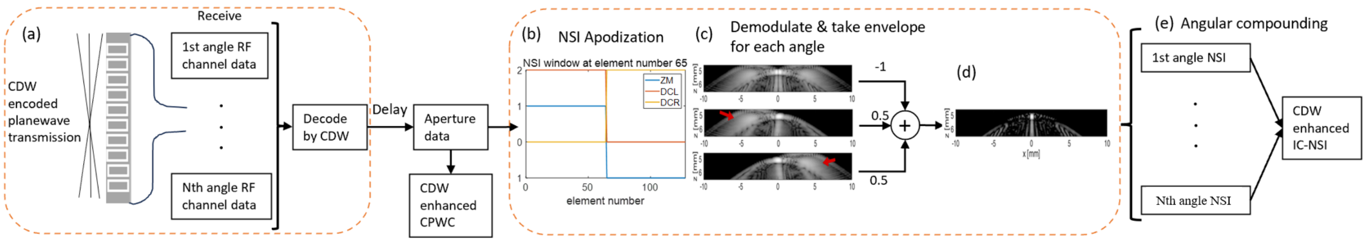

Fig. 1. Block diagram of the CDW enhanced IC-NSI imaging method, (a) CDW coded signals are transmitted and decoded first to get enhanced channel RF data. The CDW enhanced CPWC image can be obtained directly through conventional DAS and angle compounding. CDW enhanced IC-NSI is also generated using the same delay map, employing three distinct apodization windows to derive the envelope, followed by incoherent angle compounding. (b) illustrates NSI apodization windows at element 65, (c) showcases single scatterer images using ZM, DCL, and DCR, and (d) displays the resulting NSI image from a single angle by summing the three apodized images [55].

FWHM of the auto-correlation function in homogeneous regions across frames from multiple subjects were used for *in vivo* evaluation. CR and CNR are defined as follows:

$$CR = \frac{\mu_o - \mu_i}{\mu_o + \mu_i}, \quad (4)$$

$$CNR = \frac{\mu_o - \mu_i}{\sqrt{\sigma_i^2 + \sigma_o^2}}, \quad (5)$$

where μ_i and μ_o represent the mean amplitudes of the regions inside and outside the target, respectively, and σ_i and σ_o denote their corresponding standard deviations.

This study additionally used the generalized contrast-to-noise ratio (GCNR) [56] for image quality assessment. GCNR is a robust measure of lesion detectability formulated as

$$GCNR = C_0^{-\frac{C_0}{C_0 - 1}} - C_0^{-\frac{1}{C_0 - 1}}, \quad (6)$$

where C_0 is the contrast between a region of interest and the background and defined as $C_0 = \mu_i/\mu_o$, where μ_i is the average envelope level inside the region of interest, and μ_o is the average envelope level of the background.

Speckle tracking accuracy was also evaluated to assess the effect of spatial resolution. In the simulation study, mean absolute error (MAE) was adopted as the evaluation metric. It measured the difference between the estimated displacement and the ground truth displacement. In the *in vivo* study, the ground truth displacement is unavailable. Therefore, we adopted mean squared error (MSE), peak signal-to-noise ratio (PSNR), and structural similarity index measure (SSIM) [60] between pre-deformed and motion-corrected post-deformed envelope images. The motion correction process began by estimating displacement fields between pre-deformed images and post-deformed images during the cardiac cycle. Using the estimated displacement field, we then warped the post-deformation image back toward the pre-deformed geometry. MSE is a measure of the average squared difference between the original and the motion-corrected post-deformed images. PSNR is a measure of the ratio between the maximum possible power of a signal (p_{max}) and the power of noise that affects the fidelity of signal representation as follows:

$$PSNR = 10 \times log_{10}\left(\frac{{p_{max}}^2}{MSE}\right). \quad (7)$$

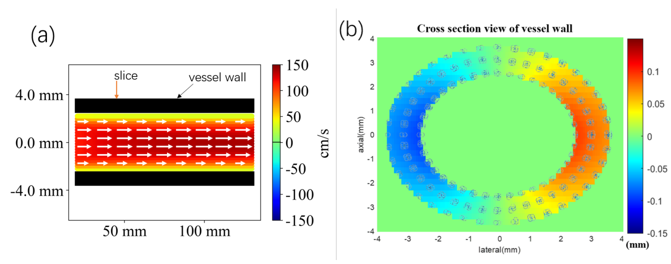

Fig. 2. A finite-element simulation of a blood vessel with blood scatterers inside: (a) shows the longitudinal plane of the simulated blood vessel. The color scale represents the lateral velocity of blood particles in units of cm/s, and the white arrows indicate both the direction and relative magnitude of blood particle velocity vectors. (b) shows a ground truth displacement map in a cross-sectional view. Blue circles represent the nodes forming the vessel wall, with positive and negative values indicating rightward and leftward motion, respectively.

SSIM is a measure of the structural similarity between the original and the estimated images and defined as:

$$SSIM\,(x, y) = \frac{(2\mu_x\mu_y + c_1)\,(2\sigma_{xy} + c_2)}{(\mu_x^2 + \mu_y^2 + c_1)\,(\sigma_x^2 + \sigma_y^2 + c_2)}, \quad (8)$$

where μ_x and μ_y are the means of the original and motion-corrected post-deformed envelope images, respectively; σ_x and σ_y are the standard deviations of the original and motion-corrected post-deformed envelope images, respectively; σ_{xy} is the covariance between the original and estimated images; c_1 and c_2 are constants for stabilizing the division and respectively defined as $c_1 = (0.01 \times L)^2$, $c_2 = (0.03 \times L)^2$, where L is the dynamic range of the envelope images. A smaller MSE, as well as a higher PSNR and a higher SSIM, indicates better estimation accuracy.

III. Experiments

A. Computer simulations

Computer simulations of arterial wall deformation were based on finite-element modeling and ultrasound image synthesis. A finite-element fluid-structure interaction model of a deforming three-dimensional (3-D) anisotropic soft tube with a blood flow inside was developed using COMSOL Multiphysics 6.0 (Burlington, MA). The tubular wall was nearly incompressible (Poisson's ratio: 0.495), had geometric parameters with reference to a realistic human common carotid artery (diameter = 5.5 mm, wall thickness = 1.22 mm with the media of 0.62 mm and adventitia of 0.6 mm) [61]. The flow velocity and blood pressure in a cardiac cycle based on the same human carotid artery defined the boundary conditions at the inlet and outlet, respectively, in the simulation. The time-dependent analysis solved for a time range of 1001 ms with a simulation time step of 100 ms. For the purpose of speckle tracking and strain imaging, a total of 11 time steps sampled at a fixed time interval were selected. The coordinates and nodal displacements of the simulated blood vessel in a cross-sectional view of interest were exported from the finite-element solutions. Figure 2(a) shows the blood flow velocity field in a finite-element simulation of a blood vessel in the longitudinal plane. Figure 2(b) shows a ground truth lateral displacement map in a cross-sectional view and the nodes that form the simulated two-layer vessel wall. Interpolation of the nodal displacements with a factor of 10 produced the full displacement field within the vessel wall.

Ultrasound images were simulated using Field II [62] and the L11-4 probe configuration, which has 128 elements, an aperture of 38 mm, and an elevational focus of 25 mm, an operating frequency of 7.2 MHz. To simulate fully developed speckle, each resolution cell had approximately 20 scatterers and thus a scatterer density of 125 per mm^3. The scatterers within the vessel wall, surrounding tissue, and lumen were all randomly distributed in space. The mean amplitudes of the surrounding tissue and blood scatterers followed Gaussian distributions and were respectively five and 50 times weaker than that of the vessel wall. The blood scatterers moved together with the inner boundary of the vessel wall within the 2D image plane and were assigned random displacements in the elevation direction within the simulated 4 mm elevational width. The surrounding tissue and blood moved in-plane with the outer and inner blood vessel walls, respectively. Five plane waves, both with and without modified 16-digit CDW, were transmitted with a steering angle spanning from $-6°$ to $6°$ at increments of $3°$. Gaussian noise of 30 dB, which was relative to simulated mean power of the received channel RF signals, was added to the RF channel data.

B. Phantom experiments

Two separate phantom experiments were conducted for image quality evaluation using a CIRS ATS Model 539 phantom. In the first set of experiments, point targets and anechoic cyst targets with a diameter of 8 mm were scanned for assessment of image quality. In the second set of phantom experiments, a homogeneous area without cyst or point targets was scanned with the probe affixed to a linear translation stage. This configuration was designed to introduce purely lateral translation from 0 to 0.9 mm at increments of 0.1 mm, to evaluate speckle coherence and lateral displacement estimation accuracy across different imaging methods in a controlled experimental setting without the signal distortion due to axial deformation. Displacement estimation was performed on images formed by CPWC, IC-NSI with DC = 1, CDW, and CDW enhanced IC-NSI with different DC offsets to investigate the effect of DC offset. Strain imaging was not evaluated in the phantom study because ground-truth strain values can hardly be obtained from phantom experiments, unlike from computer simulations.

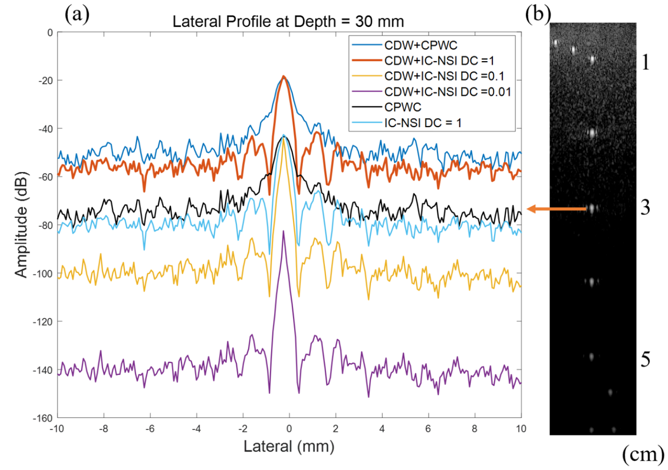

Fig. 3. (a) Lateral profiles of a wire target at depth = 30 mm in a CIRS ATS Model 539 phantom imaged by CPWC, IC-NSI, CDW-enhanced CPWC, and CDW-enhanced IC-NSI with three different DC offsets. (b) An IC-NSI (DC offset = 1) image of six wire targets in the same phantom.

For both sets of phantom experiments, their imaging setup was identical to that used in the computation simulations (section III-A). The raw RF signals were acquired using the L11-4 array probe connected to a Verasonics Vantage 256 system and driven at a voltage of 4 volts.

C. In vivo experiments

The experimental protocol for the human carotid artery was approved by the Human Research Ethics Committee at the University of Hong Kong (EA1907023) prior to ultrasound scans. The common carotid arteries of three young (27-year-old male, 25-year-old male, and 30-year-old female) healthy subjects in a transverse view were scanned in a clinical setting under the supervision and guidance of the corresponding author, who has over 10 years of experience in vascular ultrasound imaging using the same ultrasound system and imaging parameters (see section III-B). Written informed consent of the three subjects was obtained.

IV. Results

A. Image quality improvement

Figure 3 compares the lateral profiles of a wire target at 30 mm depth inside the multipurpose phantom obtained using CPWC, IC-NSI, CDW, and CDW enhanced IC-NSI with DC offsets of 1.0, 0.1 and 0.01. The data represent 10 independent acquisitions at different elevation positions of the same wire target within the CIRS phantom. The beam patterns were normalized to the maximum intensity across different imaging methods. Table I summarizes the beamwidths measured across six point targets located at different depths with the error bars representing the standard deviations (SDs). Overall, IC-NSI with DC offset = 1, 0.1, and 0.01 respectively improved lateral resolution by 42%, 84% and 88% compared to CPWC, with a lower sidelobe and a computation cost not exceeding three times that of CPWC.

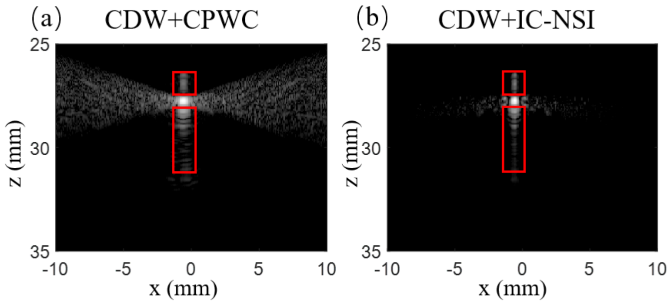

Fig. 4. Assessment of comet-tail artifacts in the case of (a) CDW and (b) CDW IC-NSI DC = 1.

There is an axial lobe artifact inherent to plane wave imaging, and an imperfect decoding in CDW may sometimes amplify this artifact. To quantitatively assess comet-tail artifacts in imaging cases with plane wave implementation, we estimated contrast ratios between the main lobe peak and artifact regions (red boxes in Fig. 4 - axial directions above/below point targets). The ghost artifact analysis revealed that CDW+IC-NSI achieved higher main-to-artifact contrast ratios than CDW+CPWC (upper artifact: 40.66 dB vs 37.67 dB; lower artifact: 41.90 dB vs 38.61 dB). These results confirmed that IC-NSI effectively mitigated ghost artifacts in CDW-enhanced plane wave imaging.

In the *in vivo* study, despite inter-subject variability, CDW-enhanced IC-NSI demonstrated an average of 38% improvement in lateral resolution compared to CDW-enhanced CPWC (Appendix B Fig. S1). This was consistent with our phantom results. The improvement was slightly reduced in deeper regions compared to shallower regions due to expected attenuation and reverberation effects.

The observation that IC-NSI with smaller DC offsets resulted in better spatial resolution but weaker signals was consistent with the literature finding [63]. CDW with 16 cascaded waves improved the SNR of IC-NSI with DC offset of 1 by 9.6 dB (Table II). CDW enhanced the SNRs of the wire target images obtained using CPWC and IC-NSI and did not affect the mainlobe beam pattern and width.

Table II summarizes CR, CNR, and GCNR values computed from hypoechoic targets (red boxes in Fig. 5) and background regions (green boxes in Fig. 5) for the four imaging methods with the error bars representing the SDs. All three metrics indicated the lowest contrast from IC-NSI among all the examined methods, but CDW significantly improved the contrast of IC-NSI with DC offset = 1, even exceeding the conventional CPWC method alone. The results collectively demonstrated that CDW-enhanced IC-NSI achieved superior lateral resolution compared to both CDW and CPWC, and it exhibited better CR, CNR, GCNR, and sSNR than IC-NSI and CPWC at the depth of 40 mm, as confirmed by statistical analysis using Welch's t-test (all p <0.05).

B. Phantom experiments with linear translation

Figure 6 shows the effect of DC offsets on speckle tracking accuracy. The mean and standard deviation were calculated by analyzing the results of multiple estimation windows in

TABLE I
LATERAL BEAMWIDTHS ACROSS SIX POINT TARGETS IN THE CIRS ATS MODEL 539 PHANTOM IMAGED WITH FOUR DIFFERENT IMAGING METHODS

Method Depth	CPWC	IC-NSI DC=1	CPWC w/CDW	IC-NSI DC=1 w/CDW	IC-NSI DC=0.1 w/CDW	IC-NSI DC=0.01 w/CDW
10mm	0.90 ± 0.062	0.38 ± 0.030	0.93 ± 0.065	0.38 ± 0.033	0.11 ± 0.020	0.10 ± 0.022
20mm	0.78 ± 0.027	0.30 ± 0.014	0.80 ± 0.025	0.31 ± 0.015	0.11 ± 0.014	0.10 ± 0.026
30mm	0.68 ± 0.015	0.38 ± 0.018	0.69 ± 0.016	0.38 ± 0.018	0.12 ± 0.019	0.10 ± 0.021
40mm	0.79 ± 0.012	0.48 ± 0.016	0.79 ± 0.012	0.48 ± 0.015	0.13 ± 0.064	0.12 ± 0.074
50mm	0.89 ± 0.013	0.59 ± 0.014	0.89 ± 0.011	0.59 ± 0.013	0.10 ± 0.026	0.09 ± 0.044
60mm	1.01 ± 0.027	0.73 ± 0.023	1.01 ± 0.014	0.72 ± 0.018	0.12 ± 0.016	0.11 ± 0.027
Mean	0.84 ± 0.026	0.48 ± 0.019	0.85 ± 0.024	0.48 ± 0.019	0.12 ± 0.030	0.11 ± 0.036

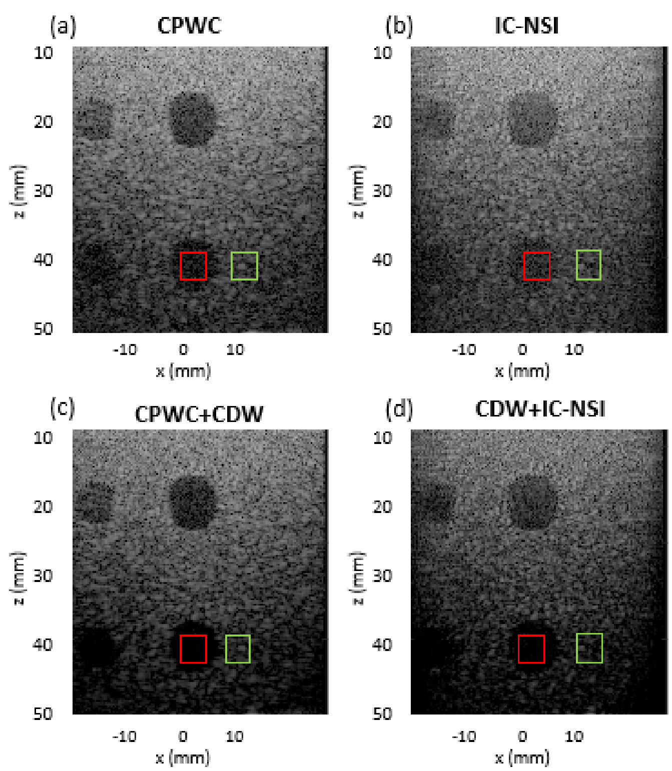

Fig. 5. Hypoechoic cyst phantom images reconstructed with (a) CPWC (b) IC-NSI (c) CDW with CPWC, and (d) CDW-enhanced IC-NSI with DC offset = 1. The dynamic range is 60 dB for all four images, which were formed with the same five steering angles of plane waves and F# =1.

the same homogeneous phantom area for different imaging methods. Correlation maps were generated using a sliding kernel of $6\lambda \times 4\lambda$ (axial $\times$ lateral). This kernel size was selected to balance the trade-off between spatial resolution and correlation accuracy given the large scale lateral linear motion present in our validation. Among those, IC-NSI with DC = 0.01 caused much larger random errors as evidenced by their large standard deviations. The MAEs for CPWC, IC-NSI with DC = 1, CDW-enhanced CPWC, and CDW-enhanced IC-

TABLE II

CONTRAST ANALYSIS OF HYPOECHOIC REGIONS IN THE CIRS ATS MODEL 539 PHANTOM IMAGED WITH FOUR DIFFERENT IMAGING METHODS

20mm	CPWC	IC-NSI DC = 1	CPWC w/CDW	IC-NSI DC = 1 w/CDW
CR	0.60 ± 0.003	0.49 ± 0.004	0.61 ± 0.001	0.51 ± 0.001
CNR	1.47 ± 0.01	1.02 ± 0.01	1.54 ± 0.003	1.08 ± 0.002
GCNR	0.47 ± 0.003	0.38 ± 0.003	0.48 ± 0.001	0.40 ± 0.001
sSNR	26.41 ± 0.26	30.17 ± 0.30	36.47 ± 0.25	40.83 ± 0.26
40mm	**CPWC**	**IC-NSI DC = 1**	**CPWC w/CDW**	**IC-NSI DC = 1 w/CDW**
CR	0.41 ± 0.01	0.27 ± 0.01	0.68 ± 0.01	0.60 ± 0.02
CNR	1.05 ± 0.05	0.68 ± 0.04	1.56 ± 0.02	1.09 ± 0.02
GCNR	0.31 ± 0.01	0.20 ± 0.01	0.55 ± 0.01	0.47 ± 0.01
sSNR	5.16 ± 0.58	9.96 ± 0.55	18.18 ± 0.30	22.33 ± 0.30

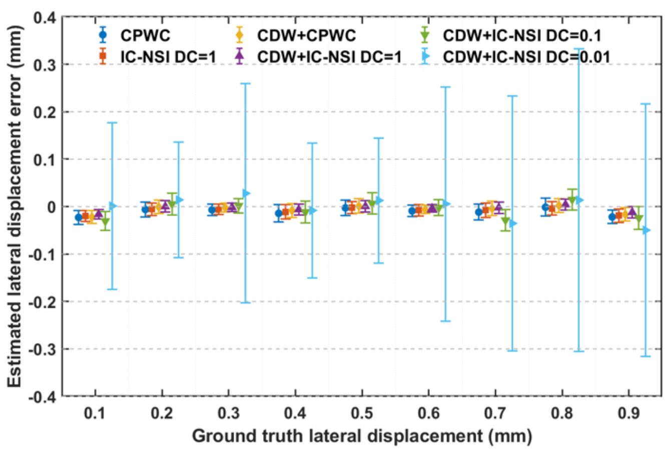

Fig. 6. Mean and standard deviations of the estimated lateral displacements error in a homogeneous phantom undergoing nine steps of pure lateral translation ranging from 0.1 mm to 0.9 mm at increments of 0.1 mm. Displacements were estimated from the images produced by CPWC, IC-NSI, CDW, and CDW enhanced IC-NSI with three different DC offsets.

NSI with DC = 1 were 0.028, 0.026, 0.019, and 0.017 mm, respectively. The results show that CDW-enhanced IC-NSI with DC = 1 reduced MAE by approximately 40% compared to the conventional CPWC method (0.017 mm vs. 0.028 mm).

Figure 7 shows inter-frame correlation maps for variant IC-NSI and benchmark CPWC methods. The overall high correlation coefficients in the cases of CPWC (Fig. 7(a), 0.84±0.06), IC-NSI with DC = 1 (Fig. 7(b), 0.83±0.05), CDW-enhanced CPWC (Fig. 7(c), 0.89±0.04), and CDW-enhanced IC-NSI with DC =1 (Fig. 7(d), 0.88±0.04) confirmed the high inter-frame similarity, thus yielding acceptable lateral displacement estimates (Fig. 6). Despite their better lateral resolution, IC-NSI with DC = 0.1 and 0.01 resulted in much lower inter-frame correlation (Fig. 7(e), 0.57±0.08 and (f), 0.43±0.10), thus hampering lateral displacement estimation. The inter-frame correlation is linked to speckle coherence, which can be quantified using speckle statistics. Unlike IC-NSI with DC = 0.1 and 0.01, the density function of the signal amplitude for IC-NSI with DC = 1 did not deviate much from that for CPWC (Fig. 8).

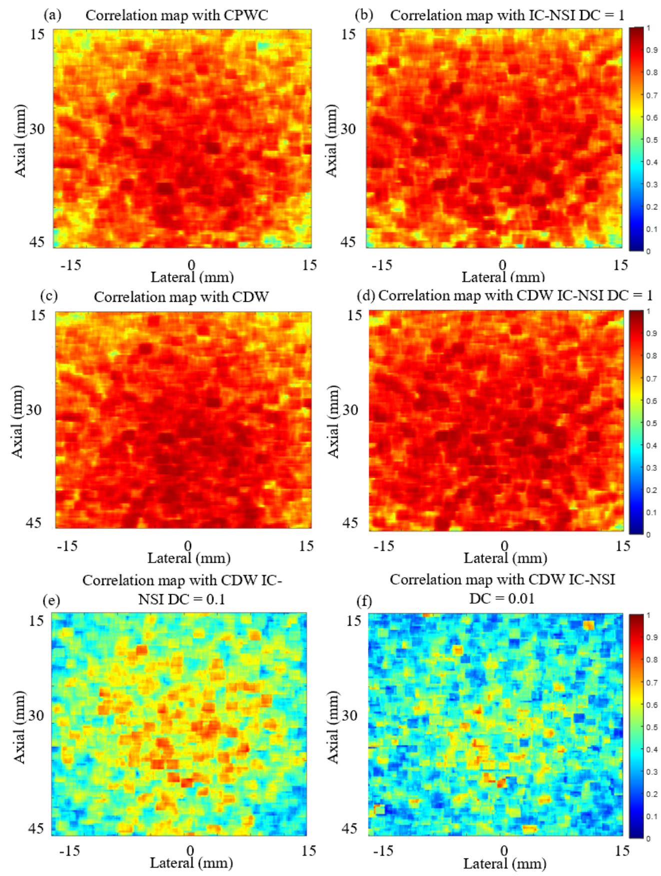

Fig. 7. Correlation maps of a homogeneous region in the CIRS phantom after a 0.2 mm linear translation, reconstructed with (a) CPWC (b) IC-NSI with DC = 1 (c) CDW with CPWC (d) CDW enhanced IC-NSI with DC = 1 (e) CDW enhanced IC-NSI with DC = 0.1, and (f) CDW enhanced IC-NSI with DC = 0.01.

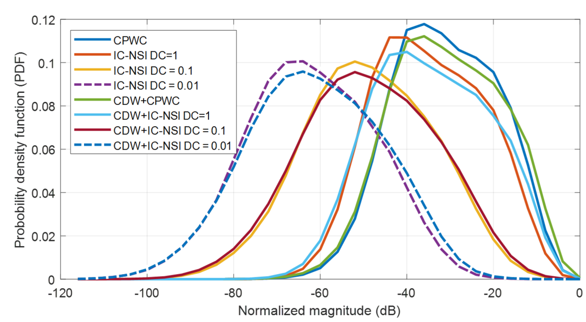

Fig. 8. Magnitude distribution of speckle statistics from experimental data acquired using a homogeneous phantom (as shown in Fig. 6) for different beamforming methods.

C. Computer simulations

Figure 9 (a) and (b) compare the B-mode images of the simulated blood vessel in the transverse view, obtained using CPWC and CDW-enhanced IC-NSI with DC = 1. Figure 9 (c) and (d) show corresponding maps of estimated lateral displacements. Positive and negative lateral displacements represent rightward and leftward motions, respectively. Fig.

This article has been accepted for publication in IEEE Transactions on Ultrasonics. This is the author's version which has not been fully edited and
content may change prior to final publication. Citation information: DOI 10.1109/TUSON.2025.3649027

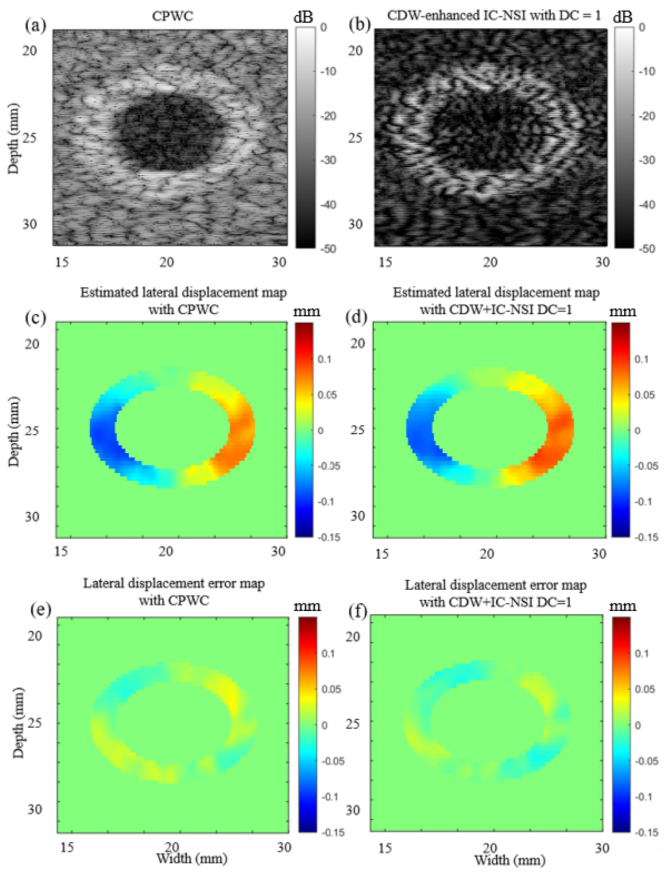

Fig. 9. Finite-element simulation of a blood vessel during dilation: (a, b) B-mode images, (c, d) estimated lateral displacement maps, and (e, f) lateral displacement estimation error maps. The left and right panels correspond to conventional CWPC and CDW enhanced IC-NSI with DC = 1, respectively. The error maps show deviations of the estimated lateral displacement fields from the ground truth.

9 (e) and (f) show lateral displacement error maps obtained by subtracting the ground truth (Fig. 2(b)) from the estimated displacements. We observed slight overestimation in the first and the third quadrants of the wall but a slight underestimation in the second and the fourth quadrants.

Figure 10 shows lateral displacement estimation errors for different pairs of comparison frames (i.e., different applied strain levels) and for two SNR levels across different imaging methods. In all pairwise comparisons, frame 0 was used as the reference frame. The MAE of lateral displacement estimation was computed by averaging the errors over all spatial positions within the region of interest for different applied strain levels. The MAE of lateral displacement estimation across all temporal steps in the case of CDW-enhanced IC-NSI was 0.0026 mm, representing a 15% reduction compared to the average MAE of 0.0031 mm achieved in the cases of CPWC-based envelope and RF data under SNR = 30 dB. Intermediate performance was observed in both cases of IC-NSI and CDW-enhanced CPWC, achieving MAE of 0.0028 mm and 0.0029 mm, respectively. At SNR = 10 dB, CDW-enhanced CPWC and IC-NSI yielded an average MAE that was 10% higher than at SNR = 30 dB.

Figure 11 compares the estimated strain maps ((b) and (c))

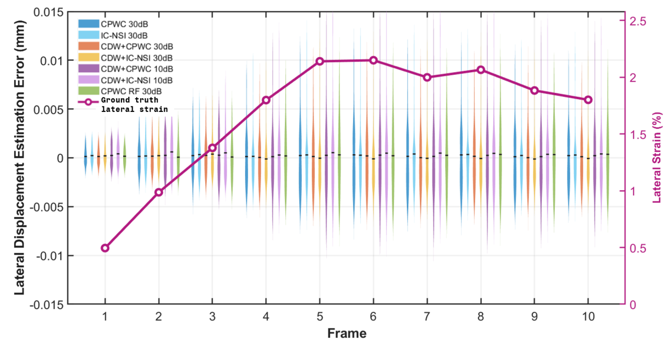

Fig. 10. Violin plots for lateral displacement estimation of the finite-element simulated blood vessel at different time steps (strain levels) in the cases of CPWC 30 dB, IC-NSI 30 dB, CDW+CPWC 30 dB, CDW+IC-NSI 30 dB, CDW+CPWC 10 dB, CDW+IC-NSI 10 dB, and CPWC RF 30 dB. The IC-NSI methods are all with DC = 1, with dB denoting the added Gaussian noise level to the RF data.

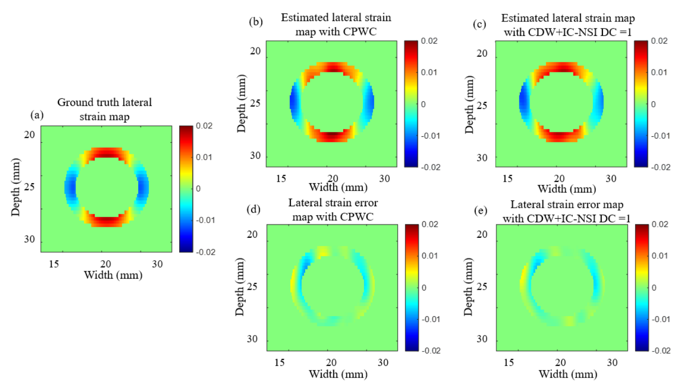

Fig. 11. Lateral strain estimation maps of the finite-element simulated blood vessel during dilation (i.e., frame 4 in Fig. 10) in the case of SNR = 30 dB. Lateral strains were computed from the 2D displacement maps obtained in the cases of (a) ground truth, (b) conventional CPWC, and (c) CDW-enhanced IC-NSI with DC = 1. Absolute difference maps show deviations from ground truth values in the cases of (d) CPWC and (e) CDW-enhanced IC-NSI with DC = 1.

derived from the displacement maps in Fig. 9(c) and (d) with the ground truth lateral strain map (Fig. 11 (a)) during dilation. Positive and negative lateral strains represent extension and compression, respectively. For a dilated blood vessel, the side walls should be compressed, whereas the upper and lower walls should be stretched in the lateral direction. Quantitative analysis for the strain error maps shown in Fig. 11(d) and (e) demonstrated that CDW-enhanced IC-NSI achieved a lower MAE of lateral strain estimates than CPWC did at time step 4 (0.19% vs, 0.23%). The strain MAE across all 10 different strain scenarios was on average reduced by 13% ± 2% in the case of CDW+IC-NSI compared to CPWC.

D. In vivo human carotid artery experiments

Figure 12 shows estimated lateral displacement (top row) and strain (bottom row) maps overlaid on the B-mode images of an *in vivo* human common carotid artery at a diastolic time point of a cardiac cycle based on the four different imaging techniques. The right and left walls of the carotid artery moved leftward and rightward, respectively, in all lateral displacement images. This indicated blood vessel recoil during diastole (Fig. 12(a)-(d)). Figure 12(e)-(h) consistently show thickening of the right arterial wall and compression of the upper arterial wall. The main discrepancies resided in the lower left segment of the arterial wall.

The temporal profiles of MSE (Fig. 13(a)), PSNR (Fig. 13(b)), and SSIM (Fig. 13(c)) show the variations in estimation accuracy associated with each method within the cardiac cycle of subject 1. The results of the other 2 subjects are provided in the Appendix C (Fig. S3 and S4). Quantitative analysis of lateral displacement accuracy from the three subjects with multiple cardiac cycles spanning 2 seconds demonstrated that CDW-enhanced IC-NSI achieved lower MSE, higher PSNR, and improved SSIM values. These improvements were more evident at the time instants after the end diastolic and at dicrotic notch phases, which corresponded to pronounced wall motion in the M-mode image (Fig. 13(d)). The motion corrected B-mode images exhibited high similarity with the pre-deformed frames during the diastolic phase, characterized by relatively small motion. The peaks of the MSE curves corresponded to the time point with pronounced wall motion and large artery wall deformation.

V. Discussion

This study presents an ultrasound strain imaging approach that integrates multi-plane wave transmissions, IC-NSI, a nonlinear beamformer, and CDW, a coded excitation method that involves only linear operations. The results showed that IC-NSI with DC offset = 1 sufficiently preserved speckle coherence needed for tissue motion estimation. The *in vitro* and *in vivo* results demonstrated that the proposed approach improved lateral resolution and sSNR. Such improvements directly contributed to the estimation of lateral displacement (*in vitro* and *in vivo*) and strain (*in silico* and *in vivo*) without a substantial increase in computational cost.

The feasibility of IC-NSI in speckle tracking was evaluated for the first time. In NSI beamforming, the DC offset is tunable, and smaller DC offsets, such as 0.1 and 0.01, yield better lateral resolution but are more sensitive to noise (Table II) and degrade speckle coherence (Fig. 7 and 8), both of which hinder speckle tracking. As demonstrated in the *in vitro* phantom results (Fig. 6), DC offset = 1 for IC-NSI should be chosen to improve lateral resolution while ensuring speckle coherence for speckle tracking tasks. As shown in both the simulation and phantom results, integrating CDW into IC-NSI mitigated SNR loss and further increased signal correlation, thereby increasing estimation accuracy (mean values in Fig. 6 and 10) and precision (standard deviations in Fig. 6 and 10) of lateral motion. This synergistic effect stems from the ability of CDW to increase signal energy through coded transmissions without compromising acquisition frame rates.

The *in vivo* feasibility of the proposed method was evaluated in the human carotid artery primarily because the thin wall structure of the artery required high spatial resolution to resolve. Meanwhile, the peak strain rates of the arterial wall during systole are generally small, with total wall deformation rarely exceeding 5% strain [64], [65], so the *in vivo* imaging frame rate requirement was rather relaxed relative to ultrafast imaging needed for blood flow imaging. It is important to note that for the *in vivo* experiments, the CDW-based method and non-CDW-based method were recorded at different time points due to the different transmission pulses. Consequently, variations in respiration and body movement may have introduced intrinsic differences in motion estimation accuracy.

The strain filter theory [66] elucidates an optimal inter-frame strain range for RF-based strain estimation. Coherent plane or diverging wave imaging makes it possible to adapt the frame rate to optimal inter-frame tissue deformation, especially for dynamic organs with large deformation. The proposed method is compatible with ultrafast imaging for high frame rate (>1000 fps) applications, such as cardiac shear wave elastography [67]. The CDW method inherently supports ultrafast frame rates, and the number of cascaded waves can flexibly adapt to the minimum requirement of image quality for speckle tracking and strain imaging. NSI, as a post-processing technique, operates entirely on beamformed data and is independent of the hardware or acquisition scheme. This separation allows NSI to improve lateral resolution after data collection by narrowing the beamwidth (Fig. 3) without altering pulse sequences or transducer configurations. The CDW-enhanced IC-NSI introduces only linear mathematical operations, resulting in a total processing load less than 3× that of CPWC. This contrasts with methods, like MV and DMAS, which increase computation cost during beamforing, limiting scalability.

There are several study limitations. One is the use of envelope data for speckle tracking. The envelope signal, while useful for motion estimation, lacks the phase information, which is present in the RF signal and crucial for accurate axial displacement estimation. Currently, the NSI technique does not support beamformed RF signals. Future work shall consider combining RF-based axial tracking with our lateral enhancement strategy or developing a new RF-based NSI framework that can keep the phase information. Although not shown, radial and circumferential strains are typically derived from lateral, axial, and shear strains, which are computed from lateral and axial displacement estimation. Our study hypothesis is that the proposed method improves lateral displacement estimation and thus 2D strain estimation, regardless of the Cartesian or polar coordinate system.

The observed improvements in lateral displacement estimation and derived strain maps are critical for resolving subtle structural and mechanical heterogeneities within biological tissues. Particularly in vascular applications, this improved fidelity allows for more accurate characterization of plaque biomechanics—such as distinguishing a stiff fibrous cap from a soft lipid pool or identifying localized stiffening—thereby improving the assessment of plaque vulnerability and stroke risk. Although this study demonstrates the principle in a healthy vessel, the improved spatial fidelity in lateral strain estimation aims to enable characterization of vascular pathology, where accurately resolving mechanical heterogeneities is crucial for diagnosis. Furthermore, the method's compatibility with higher-frequency ultrasound array imaging suggests potential for achieving even finer resolution in various clinical applications.

Looking ahead, as USI serves as a pivotal tool for quantify-

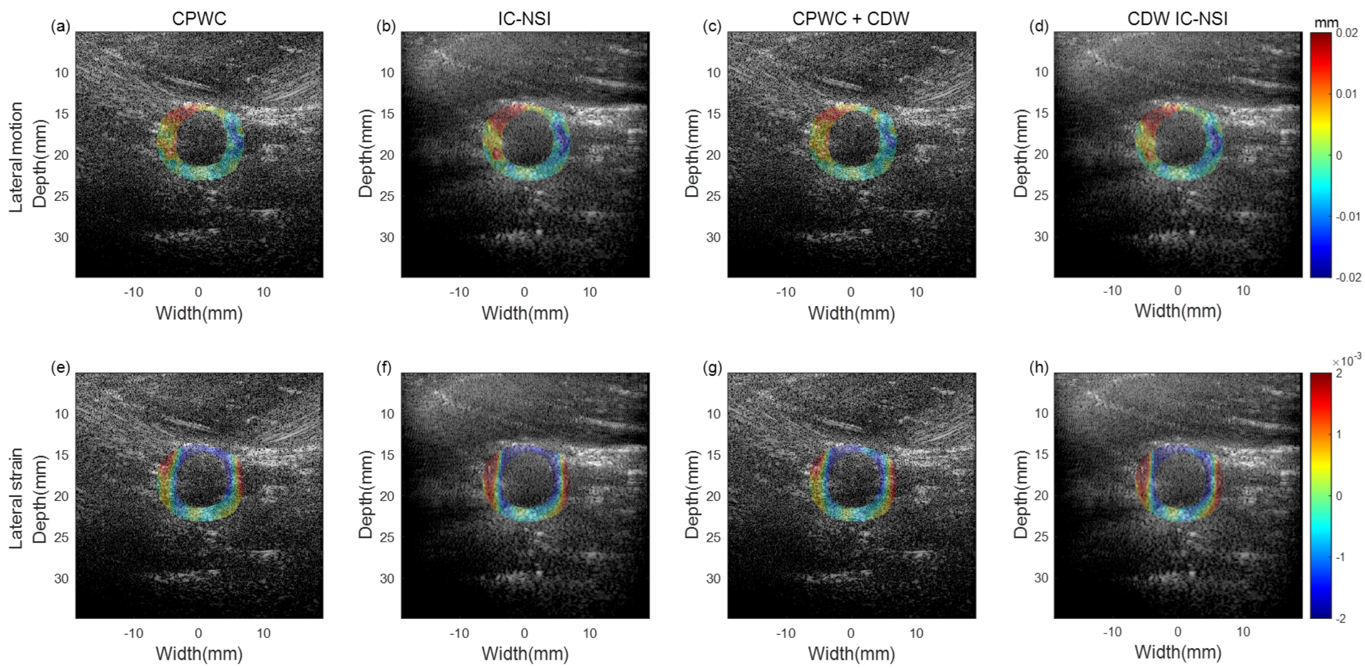

Fig. 12. Estimated lateral displacement (top) and strain (bottom) maps overlaid on the B-mode images of the carotid artery of a healthy human subject *in vivo* in a transverse view at a diastolic time point in the cardiac cycle in the cases of (a, e) CPWC, (b, f) IC-NSI with DC = 1, (c, g) CDW-enhanced CPWC, and (d, h) CDW enhanced IC-NSI with DC = 1.

ing biological soft tissue deformation, future research trajectories could focus on exploring the method's applicability across a broader range of tissue types and clinical scenarios, such as aortas and skeletal muscle, given that the proposed framework addresses challenges related to lateral resolution, contrast, and penetration depth. NSI effectively suppresses the sidelobe and grating lobes, so it may be possible to use larger pitch transducers while still maintaining reliable motion and strain estimation. Furthermore, using ultrafast frame rates will allow for more accurate motion estimation of drastically deforming biological tissues and fully leverage the high resolution and low computational cost of the proposed method. Frame rates on the order of hundreds to thousands per second can reduce signal decorrelation and facilitate applications that rely on time-ensemble estimation using multiple successive frames.

The characteristics of the lateral direction in 2D ultrasound imaging also apply to the elevational direction in 3D ultrasound. The proposed method can be extended to 3D ultrasound imaging and is anticipated to hold potential for further advancements in fast 3D ultrasound strain imaging.

VI. Conclusion

This work introduced and assessed the performance of CDW, a linear coded excitation scheme, in conjunction with IC-NSI, a nonlinear beamformer, for high-quality 2D motion estimation and USI. The proposed ultrasound imaging method enhanced lateral resolution and contrast at a desired frame rate while maintaining low computational complexity. The improved resolution and contrast were proven to be indispensable for ameliorating lateral motion estimation and strain imaging, which is the fundamental challenge in USI. Validation through simulations as well as experiments on a tissue-mimicking quality assurance phantom and the *in vivo* human common carotid artery substantiated the effectiveness of the proposed method. The CDW-enhanced IC-NSI with DC offset = 1 is expected to be a viable imaging method for biological tissues that require high image resolution and contrast at a tunable frame rate for motion and strain analysis, such as the major arteries in the circulation system.

Acknowledgment

The authors would like to thank Dr. Yuchen Tang and Dr. Yue Xu for their help with the in vitro experiments.

References

[1] M. Bertrand, J. Meunier, M. Doucet, and G. Ferland, "Ultrasonic biomechanical strain gauge based on speckle tracking," in *Proceedings., IEEE Ultrasonics Symposium,*, pp. 859–863, IEEE, 1989.

[2] M. O'Donnell, A. R. Skovoroda, B. M. Shapo, and S. Y. Emelianov, "Internal displacement and strain imaging using ultrasonic speckle tracking," *IEEE transactions on ultrasonics, ferroelectrics, and frequency control*, vol. 41, no. 3, pp. 314–325, 1994.

[3] J. Ophir, I. Cespedes, H. Ponnekanti, Y. Yazdi, and X. Li, "Elastography: a quantitative method for imaging the elasticity of biological tissues," *Ultrasonic imaging*, vol. 13, no. 2, pp. 111–134, 1991.

[4] M. Ashikuzzaman, T. J. Hall, and H. Rivaz, "Incorporating gradient similarity for robust time delay estimation in ultrasound elastography," *IEEE Transactions on Ultrasonics, Ferroelectrics, and Frequency Control*, vol. 69, no. 5, pp. 1738–1750, 2022.

[5] M. Ashikuzzaman and H. Rivaz, "Second-order ultrasound elastography with l1-norm spatial regularization," *IEEE Transactions on Ultrasonics, Ferroelectrics, and Frequency Control*, vol. 69, no. 3, pp. 1008–1019, 2022.

[6] H. Morikawa, K. Fukuda, S. Kobayashi, H. Fujii, S. Iwai, M. Enomoto, A. Tamori, H. Sakaguchi, and N. Kawada, "Real-time tissue elastography as a tool for the noninvasive assessment of liver stiffness in patients with chronic hepatitis c," *Journal of gastroenterology*, vol. 46, pp. 350–358, 2011.

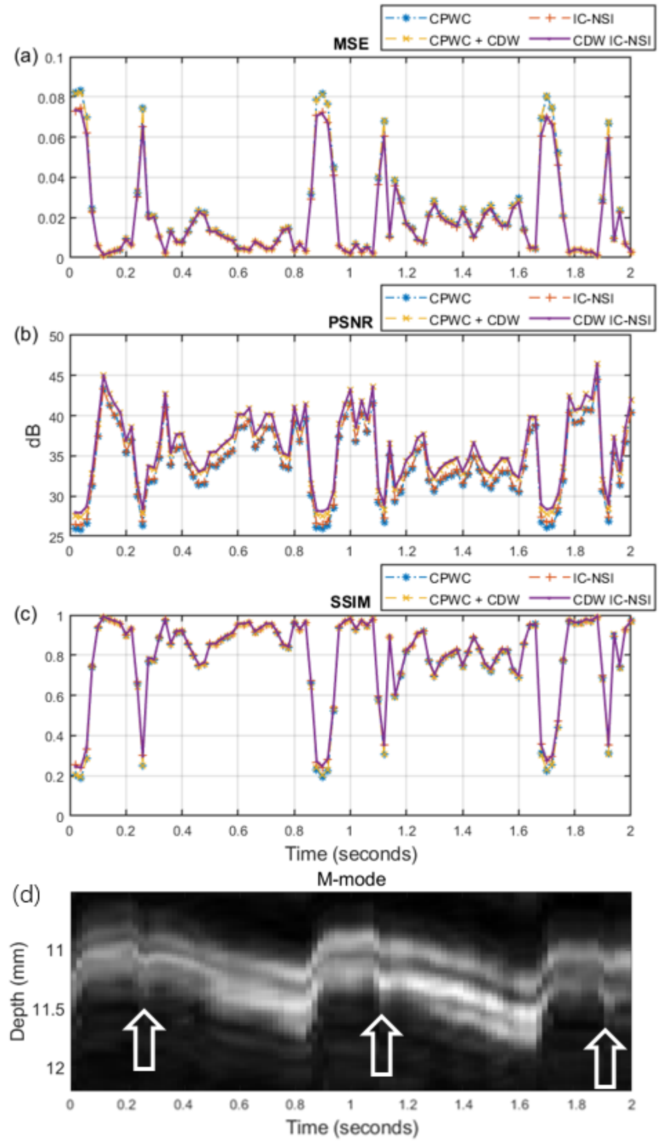

Fig. 13. Quantitative analysis of the lateral displacement accuracy for *in vivo* carotid artery image data of the same human subject shown in Fig. 12 acquired at a frame rate of 50 Hz for two seconds: the temporal profiles of (a) mean squared error (MSE), (b) peak SNR, (c) structural similarity index (SSIM), and (d) a corresponding M-mode image of the carotid artery. Note that the metrics were computed from the arterial wall regions in the pre-deformed and motion-corrected post-deformed images. White arrows indicate the dicrotic notch.

[7] I. Peride, D. Rădulescu, A. Niculae, V. Ene, O. G. Bratu, and I. A. Checheriță, "Value of ultrasound elastography in the diagnosis of native kidney fibrosis.," *Medical ultrasonography*, vol. 18, no. 3, pp. 362–369, 2016.

[8] O. A. Smiseth, H. Torp, A. Opdahl, K. H. Haugaa, and S. Urheim, "Myocardial strain imaging: how useful is it in clinical decision making?," *European heart journal*, vol. 37, no. 15, pp. 1196–1207, 2016.

[9] R. Jasaityte, B. Heyde, and J. D'hooge, "Current state of three-dimensional myocardial strain estimation using echocardiography," *Journal of the American Society of Echocardiography*, vol. 26, no. 1, pp. 15–28, 2013.

[10] H. Li, J. Poree, B. Chayer, M.-H. R. Cardinal, and G. Cloutier, "Parameterized strain estimation for vascular ultrasound elastography with sparse representation," *IEEE Transactions on Medical Imaging*, vol. 39, no. 12, pp. 3788–3800, 2020.

[11] R. S. Witte, K. Kim, B. J. Martin, and M. O'Donnell, "Effect of fatigue on muscle elasticity in the human forearm using ultrasound strain imaging," in *2006 International Conference of the IEEE Engineering in Medicine and Biology Society*, pp. 4490–4493, IEEE, 2006.

[12] R. G. Lopata, J. P. van Dijk, S. Pillen, M. M. Nillesen, H. Maas, J. M. Thijssen, D. F. Stegeman, and C. L. de Korte, "Dynamic imaging of skeletal muscle contraction in three orthogonal directions," *Journal of Applied Physiology*, vol. 109, no. 3, pp. 906–915, 2010.

[13] J. D'hooge, B. Bijnens, J. Thoen, F. Van de Werf, G. R. Sutherland, and P. Suetens, "Echocardiographic strain and strain-rate imaging: a new tool to study regional myocardial function," *IEEE transactions on medical imaging*, vol. 21, no. 9, pp. 1022–1030, 2002.

[14] E. E. Konofagou, J. D'hooge, and J. Ophir, "Myocardial elastography—a feasibility study in vivo," *Ultrasound in medicine & biology*, vol. 28, no. 4, pp. 475–482, 2002.

[15] J. Porée, D. Garcia, B. Chayer, J. Ohayon, and G. Cloutier, "Noninvasive vascular elastography with plane strain incompressibility assumption using ultrafast coherent compound plane wave imaging," *IEEE transactions on medical imaging*, vol. 34, no. 12, pp. 2618–2631, 2015.

[16] R. L. Chimenti, A. S. Flemister, J. Ketz, M. Bucklin, M. R. Buckley, and M. S. Richards, "Ultrasound strain mapping of achilles tendon compressive strain patterns during dorsiflexion," *Journal of biomechanics*, vol. 49, no. 1, pp. 39–44, 2016.

[17] M. H. R. Khan and R. Righetti, "Ultrasound estimation of strain time constant and vascular permeability in tumors using a ceemdan and linear regression-based method," *Computers in Biology and Medicine*, vol. 148, p. 105707, 2022.

[18] W. F. Walker and G. E. Trahey, "A fundamental limit on delay estimation using partially correlated speckle signals," *IEEE transactions on ultrasonics, ferroelectrics, and frequency control*, vol. 42, no. 2, pp. 301–308, 1995.

[19] S. Park, S. R. Aglyamov, W. G. Scott, and S. Y. Emelianov, "Strain imaging using conventional and ultrafast ultrasound imaging: Numerical analysis," *IEEE transactions on ultrasonics, ferroelectrics, and frequency control*, vol. 54, no. 5, pp. 987–995, 2007.

[20] O. A. Smiseth, O. Rider, M. Cvijic, L. Valkovič, E. W. Remme, and J.-U. Voigt, "Myocardial strain imaging: theory, current practice, and the future," *JACC: Cardiovascular Imaging*, 2024.

[21] H. de Hoop, N. J. Petterson, F. N. van de Vosse, M. R. van Sambeek, H.-M. Schwab, and R. G. Lopata, "Multiperspective ultrasound strain imaging of the abdominal aorta," *IEEE Transactions on Medical Imaging*, vol. 39, no. 11, pp. 3714–3724, 2020.

[22] J. Luo and E. E. Konofagou, "Effects of various parameters on lateral displacement estimation in ultrasound elastography," *Ultrasound in medicine & biology*, vol. 35, no. 8, pp. 1352–1366, 2009.

[23] J. El Harake, C. Lee, A. W. Ying, P. Gami, and E. Konofagou, "Sliding window beamforming enhances speckle resolution in high frame rate imaging," in *2023 IEEE International Ultrasonics Symposium (IUS)*, pp. 1–4, IEEE, 2023.

[24] J. Luo, W.-N. Lee, and E. E. Konofagou, "Fundamental performance assessment of 2-d myocardial elastography in a phased-array configuration," *IEEE transactions on ultrasonics, ferroelectrics, and frequency control*, vol. 56, no. 10, pp. 2320–2327, 2009.

[25] M. Ashikuzzaman, A. Héroux, A. Tang, G. Cloutier, and H. Rivaz, "Displacement tracking techniques in ultrasound elastography: From cross-correlation to deep learning," *IEEE Transactions on Ultrasonics, Ferroelectrics, and Frequency Control*, 2024.

[26] B. Dai, S. Babaei, C. K. Abbey, and M. F. Insana, "Registration methods in power doppler ultrasound for peripheral perfusion imaging," in *Medical Imaging 2022: Ultrasonic Imaging and Tomography*, vol. 12038, pp. 85–99, SPIE, 2022.

[27] E. Konofagou and J. Ophir, "A new elastographic method for estimation and imaging of lateral displacements, lateral strains, corrected axial strains and poisson's ratios in tissues," *Ultrasound in medicine & biology*, vol. 24, no. 8, pp. 1183–1199, 1998.

[28] W.-N. Lee, C. M. Ingrassia, K. D. Costa, J. W. Holmes, E. E. Konofagou, *et al.*, "Theoretical quality assessment of myocardial elastography with in vivo validation," *ieee transactions on ultrasonics, ferroelectrics, and frequency control*, vol. 54, no. 11, pp. 2233–2245, 2007.

[29] H. Peng, J. Tie, and D. Guo, "An iterative axial and lateral ultrasound strain estimator using subband division," *Journal of Medical Imaging and Health Informatics*, vol. 10, no. 5, pp. 1057–1068, 2020.

[30] Z. Liu, Q. He, and J. Luo, "Spatial angular compounding with affine-model-based optical flow for improvement of motion estimation," *IEEE Transactions on Ultrasonics, Ferroelectrics, and Frequency Control*, vol. 66, no. 4, pp. 701–716, 2019.

[31] M. Ashikuzzaman, J. Huang, S. Bonwit, A. Etemadimanesh, P. Raghavan, and M. A. L. Bell, "Displacement tracking reliability in muscle

shear strain quantification," in *Medical Imaging 2024: Ultrasonic Imaging and Tomography*, vol. 12932, pp. 66–71, SPIE, 2024.

[32] E. Brusseau, J. Kybic, J.-F. Déprez, and O. Basset, "2-d locally regularized tissue strain estimation from radio-frequency ultrasound images: Theoretical developments and results on experimental data," *IEEE Transactions on Medical Imaging*, vol. 27, no. 2, pp. 145–160, 2008.

[33] J. Jiang and T. J. Hall, "A coupled subsample displacement estimation method for ultrasound-based strain elastography," *Physics in Medicine & Biology*, vol. 60, no. 21, p. 8347, 2015.

[34] L. Guo, Y. Xu, Z. Xu, and J. Jiang, "A pde-based regularization algorithm toward reducing speckle tracking noise: A feasibility study for ultrasound breast elastography," *Ultrasonic imaging*, vol. 37, no. 4, pp. 277–293, 2015.

[35] H. Rivaz, E. M. Boctor, M. A. Choti, and G. D. Hager, "Ultrasound elastography using multiple images," *Medical image analysis*, vol. 18, no. 2, pp. 314–329, 2014.

[36] M. Ashikuzzaman, A. Sharma, N. Venkatayogi, E. Oluyemi, K. Myers, E. Ambinder, H. Rivaz, and M. A. L. Bell, "Mixture: L1-norm-based mixed second-order continuity in strain tensor ultrasound elastography," *IEEE Transactions on Ultrasonics, Ferroelectrics, and Frequency Control*, 2024.

[37] Z. Gao, S. Wu, Z. Liu, J. Luo, H. Zhang, M. Gong, and S. Li, "Learning the implicit strain reconstruction in ultrasound elastography using privileged information," *Medical image analysis*, vol. 58, p. 101534, 2019.

[38] B. Peng, Y. Xian, Q. Zhang, and J. Jiang, "Neural-network-based motion tracking for breast ultrasound strain elastography: An initial assessment of performance and feasibility," *Ultrasonic imaging*, vol. 42, no. 2, pp. 74–91, 2020.

[39] E. Evain, Y. Sun, K. Faraz, D. Garcia, E. Saloux, B. L. Gerber, M. De Craene, and O. Bernard, "Motion estimation by deep learning in 2d echocardiography: synthetic dataset and validation," *IEEE transactions on medical imaging*, vol. 41, no. 8, pp. 1911–1924, 2022.

[40] Y. Wang, J. Ghaboussi, C. Hoerig, and M. F. Insana, "A data-driven approach to characterizing nonlinear elastic behavior of soft materials," *Journal of the mechanical behavior of biomedical materials*, vol. 130, p. 105178, 2022.

[41] S. Majumder, M. T. Islam, and R. Righetti, "Raft-usenet: A unified network for accurate axial and lateral motion estimation in ultrasound elastography imaging," *IEEE Journal of Biomedical and Health Informatics*, 2025.

[42] M. Ashikuzzaman, A. K. Tehrani, and H. Rivaz, "Exploiting mechanics-based priors for lateral displacement estimation in ultrasound elastography," *IEEE Transactions on Medical Imaging*, vol. 42, no. 11, pp. 3307–3322, 2023.

[43] A. K. Tehrani, M. Ashikuzzaman, and H. Rivaz, "Lateral strain imaging using self-supervised and physically inspired constraints in unsupervised regularized elastography," *IEEE Transactions on Medical Imaging*, vol. 42, no. 5, pp. 1462–1471, 2022.

[44] Y. Wang, C. Hoerig, J. Ghaboussi, and M. Insana, "A soft-computational method for imaging nonlinear mechanical properties of tissue-like media using ultrasound," *The Journal of the Acoustical Society of America*, vol. 148, no. 4_Supplement, pp. 2522–2522, 2020.

[45] M. H. R. Khan and R. Righetti, "A novel poroelastography method for high-quality estimation of lateral strain, solid stress and fluid pressure in vivo," *IEEE Transactions on Medical Imaging*, 2024.

[46] M. Mirzaei, A. Asif, and H. Rivaz, "Virtual source synthetic aperture for accurate lateral displacement estimation in ultrasound elastography," *IEEE Transactions on Ultrasonics, Ferroelectrics, and Frequency Control*, vol. 68, no. 5, pp. 1687–1695, 2020.

[47] Y. Wang, X. Xie, Q. He, H. Liao, H. Zhang, and J. Luo, "Hadamard-encoded synthetic transmit aperture imaging for improved lateral motion estimation in ultrasound elastography," *IEEE Transactions on Ultrasonics, Ferroelectrics, and Frequency Control*, vol. 69, no. 4, pp. 1204–1218, 2022.

[48] S. Selladurai and A. K. Thittai, "Strategies to obtain subpitch precision in lateral motion estimation in ultrasound elastography," *IEEE transactions on ultrasonics, ferroelectrics, and frequency control*, vol. 65, no. 3, pp. 448–456, 2018.

[49] H. Khodadadi, A. G. Aghdam, and H. Rivaz, "Direct strain estimation in ultrasound elastography using a novel dynamic programming approach," in *2018 IEEE 15th International Symposium on Biomedical Imaging (ISBI 2018)*, pp. 1182–1186, IEEE, 2018.

[50] G. Montaldo, M. Tanter, J. Bercoff, N. Benech, and M. Fink, "Coherent plane-wave compounding for very high frame rate ultrasonography and transient elastography," *IEEE transactions on ultrasonics, ferroelectrics, and frequency control*, vol. 56, no. 3, pp. 489–506, 2009.

[51] P.-C. Li and M.-L. Li, "Adaptive imaging using the generalized coherence factor," *IEEE transactions on ultrasonics, ferroelectrics, and frequency control*, vol. 50, no. 2, pp. 128–141, 2003.

[52] J. F. Synnevag, A. Austeng, and S. Holm, "Adaptive beamforming applied to medical ultrasound imaging," *IEEE transactions on ultrasonics, ferroelectrics, and frequency control*, vol. 54, no. 8, pp. 1606–1613, 2007.

[53] G. Matrone, A. S. Savoia, G. Caliano, and G. Magenes, "The delay multiply and sum beamforming algorithm in ultrasound b-mode medical imaging," *IEEE transactions on medical imaging*, vol. 34, no. 4, pp. 940–949, 2014.

[54] M. Polichetti, F. Varray, J.-C. Béra, C. Cachard, and B. Nicolas, "A nonlinear beamformer based on p-th root compression—application to plane wave ultrasound imaging," *Applied Sciences*, vol. 8, no. 4, p. 599, 2018.

[55] Z. Kou, R. J. Miller, and M. L. Oelze, "Grating lobe reduction in plane-wave imaging with angular compounding using subtraction of coherent signals," *IEEE transactions on ultrasonics, ferroelectrics, and frequency control*, vol. 69, no. 12, pp. 3308–3316, 2022.

[56] Y. Zhang, Y. Guo, and W.-N. Lee, "Ultrafast ultrasound imaging with cascaded dual-polarity waves," *IEEE Transactions on Medical Imaging*, vol. 37, no. 4, pp. 906–917, 2017.

[57] P. Verma and M. M. Doyley, "Revisiting the cramér rao lower bound for elastography: Predicting the performance of axial, lateral and polar strain elastograms," *Ultrasound in medicine & biology*, vol. 43, no. 9, pp. 1780–1796, 2017.

[58] M. F. Insana, B. Dai, S. Babaei, and C. K. Abbey, "Combining spatial registration with clutter filtering for power-doppler imaging in peripheral perfusion applications," *IEEE transactions on ultrasonics, ferroelectrics, and frequency control*, vol. 69, no. 12, pp. 3243–3254, 2022.

[59] A. Agarwal, J. Reeg, A. S. Podkowa, and M. L. Oelze, "Improving spatial resolution using incoherent subtraction of receive beams having different apodizations," *IEEE transactions on ultrasonics, ferroelectrics, and frequency control*, vol. 66, no. 1, pp. 5–17, 2018.

[60] Z. Wang, A. C. Bovik, H. R. Sheikh, and E. P. Simoncelli, "Image quality assessment: from error visibility to structural similarity," *IEEE transactions on image processing*, vol. 13, no. 4, pp. 600–612, 2004.

[61] D. Ran, J. Dong, H. Li, and W.-N. Lee, "Spontaneous extension wave for in vivo assessment of arterial wall anisotropy," *American Journal of Physiology-Heart and Circulatory Physiology*, vol. 320, no. 6, pp. H2429–H2437, 2021.

[62] J. A. Jensen, "Field: A program for simulating ultrasound systems," *Medical & Biological Engineering & Computing*, vol. 34, no. sup. 1, pp. 351–353, 1997.

[63] Z. Kou, M. Lowerison, Q. You, Y. Wang, P. Song, and M. L. Oelze, "High-resolution power doppler using null subtraction imaging," *IEEE transactions on medical imaging*, 2024.

[64] H. Iino, T. Okano, M. Daimon, K. Sasaki, M. Chigira, T. Nakao, Y. Mizuno, T. Yamazaki, M. Kurano, Y. Yatomi, *et al.*, "Usefulness of carotid arterial strain values for evaluating the arteriosclerosis," *Journal of Atherosclerosis and Thrombosis*, vol. 26, no. 5, pp. 476–487, 2019.

[65] S. F. Arnăutu, V. I. Morariu, D. A. Arnăutu, and M. C. Tomescu, "The predictive value of carotid artery strain and strain-rate in assessing the 3-year risk for stroke and acute coronary syndrome in patients with metabolic syndrome," *Reviews in Cardiovascular Medicine*, vol. 23, no. 4, p. 146, 2022.

[66] T. Varghese and J. Ophir, "A theoretical framework for performance characterization of elastography: The strain filter," *IEEE transactions on ultrasonics, ferroelectrics, and frequency control*, vol. 44, no. 1, pp. 164–172, 1997.

[67] M. Pernot, M. Couade, P. Mateo, B. Crozatier, R. Fischmeister, and M. Tanter, "Real-time assessment of myocardial contractility using shear wave imaging," *Journal of the American College of Cardiology*, vol. 58, no. 1, pp. 65–72, 2011.

This article has been accepted for publication in IEEE Transactions on Ultrasonics. This is the author's version which has not been fully edited and content may change prior to final publication. Citation information: DOI 10.1109/TUSON.2025.3649027

Bingze Dai (Student member, IEEE) earned his B.S. degree in Electronic and Information Engineering from Beijing Institute of Technology and M.S. degree in Electrical and Computer Engineering from the University of California, San Diego and the University of Illinois at Urbana Champaign. He is currently pursuing the Ph.D. degree in Electrical and Electronics Engineering at The University of Hong Kong.

His current research interests include ultrafast ultrasound imaging, beamforming, and cardiovascular imaging.

Zhengchang Kou (Member, IEEE) earned his B.S., M.S., and Ph.D. degrees in Electrical and Computer Engineering from the University of Illinois Urbana-Champaign in 2017, 2020, and 2023, respectively. He is currently a Postdoctoral Research Associate at the Beckman Institute for Advanced Science and Technology, supported by the Beckman Institute Postdoctoral Fellowship. His research focuses on ultrafast ultrasound imaging, contrast-free super-resolution imaging, FPGA-based hardware acceleration, ultrasound imaging systems, and wearable ultrasound technologies.

Jiajing Zhang received the B.Eng. degree in biomedical engineering from Sun Yat-sen University, Guangzhou, China, in 2023. He is currently pursuing the Ph.D. degree with the Department of Electrical and Electronic Engineering, The University of Hong Kong, Hong Kong.

Haotian Guan (Student Member, IEEE) received the B. S. degree in Applied Mathematics from University of New Hampshire, Durham, NH, United States in 2018, and M.S. in Data Science from New York University, NY, United States in 2021. He is currently pursuing the Ph.D. degree with the Department of Electrical and Electronics Engineering, The University of Hong Kong.

His current research interests include physics-informed neural network for medical images and multi-modality learning.

Michael L. Oelze (M'03–SM'09) was born in Hamilton, New Zealand, in 1971. He received the B.S. degree in physics and mathematics from Harding University, Searcy, AR, USA, in 1994, and the Ph.D. degree in physics from the University of Mississippi, Oxford, MS, USA. From 2000 to 2002, he was a Post-Doctoral Researcher with the Bioacoustics Research Laboratory, Department of Electrical and Computer Engineering (ECE), University of Illinois at Urbana– Champaign (UIUC), Urbana, IL, USA. From 2002 to 2004, he was an NIH Fellow conducting research in quantitative ultrasound techniques for biomedical ultrasound applications in cancer detection. In 2005, he joined the Faculty of ECE, UIUC. He is currently a Professor in ECE, a Health Innovator Professor in the Carle Illinois College of Medicine and the Frederick G. and Elizabeth H. Nearing Scholar, Grainger College of Engineering. His research interests include biomedical ultrasound, quantitative ultrasound imaging for improving cancer diagnostics and monitoring therapy response, ultrasound tomography, ultrasound-based therapy, beamforming, coded excitation, communications using ultrasound, in body devices, and hardware solutions. Dr. Oelze is currently a Fellow of the AIUM and a Fellow of ASA. He is a member of the Technical Program Committee of the IEEE Ultrasonics Symposium. He currently serves as an Associate Editor for IEEE TRANSACTIONS ON ULTRASONICS, FERROELECTRICS, AND FREQUENCY CONTROL, Ultrasonic Imaging, and IEEE TRANSACTIONS ON BIOMEDICAL ENGINEERING.

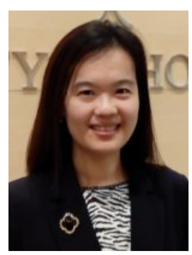

Wei-Ning Lee Wei-Ning Lee (Member, IEEE) received the B.S. and M.S. degrees in electrical engineering from National Taiwan University, Taipei, Taiwan, and the Ph.D. degree in biomedical engineering from Columbia University, New York, NY, USA. After working as a Postdoctoral Fellow at the Institut Langevin, ESPCI ParisTech, Paris, France, she joined as an Assistant Professor with the Department of Electrical and Electronic Engineering, The University of Hong Kong, Hong Kong, where she is currently an Associate Professor with tenure. Her current research interests focus on functional ultrafast ultrasound imaging methods to investigate microstructure, mechanics, and hemodynamics of cardiovascular and musculoskeletal tissues.

Dr. Lee won the New Investigator Award at the American Institute of Ultrasound in Medicine (AIUM) Annual Convention in 2009 and received an Early Career Award from the Hong Kong Research Grands Council in 2013 and Healthy Longevity Catalyst Award (Hong Kong) in 2022. She currently serves on the Editorial Board for Physics in Medicine and Biology and the Advisory Editorial Board for Ultrasound in Medicine and Biology. She is currently an Associate Editor of IEEE TRANSACTIONS ON MEDICAL IMAGING.